Magnetotransport phenomena in periodically δ-doped structures

Th. Ihn,* K.J. Friedland, and R. Hey
Paul-Drude-Institut für Festkörperelektronik,
Hausvogteiplatz 5-7, D-10117 Berlin, Federal Republic of Germany

F. Koch
Physik Department E16, Technical University of Munich,
James-Franck-Strasse, D-85748 Garching, Federal Republic of Germany
(Received 6 March 1995)

The low-temperature magnetotransport properties of δ-doped multilayers have been measured in magnetic fields up to 14 T. A set of three GaAs samples is presented with sheet-doping concentrations in the dilute metallic region and sheet distances varying between 17 nm (aspect ratio 1) and 100 nm (aspect ratio 0.14). Self-consistent calculations are used to determine the subband energies, the total density of states, and the spatial extension of electron densities in different subbands. Three transport phenomena are discussed: the classical magnetoresistance for a two-carrier system, the Shubnikov–de Haas oscillations, and the quantum Hall effect. Reduced sheet distance is found to decrease the number of occupied minibands. The miniband which is closest to the Fermi energy undergoes a transition to an anisotropic three-dimensional band with renormalized mass in the growth direction, which is a direct consequence of the periodic doping.

I. INTRODUCTION

In doped semiconductors in the metallic range of doping concentrations, the conductivity is reduced by scattering. The mobile carriers scatter at the screened potentials of the charged dopant ions, which are distributed randomly. It was suggested that an ordered lattice of dopants would overcome this disadvantage achieving a periodical doping structure without any scattering in the best case.[1] From this point of view, the periodically δ-doped multilayer with a metallic sheet-doping concentration is of special interest. It can be regarded as a first step toward the perfectly ordered doping structure, since doping is periodically ordered in the growth direction. We investigated the consequences of this kind of dopant order and will present the results in this paper.

In metallic δ-doped layers, the electrons move in a self-consistent V-shaped potential. Two-dimensional subband states form and the electron density is confined to a region with a thickness of about a Bohr radius ($a_B^* = 10$ nm) around the doping plane.[2] The higher the sheet-doping concentration, the more subbands are occupied. In a multilayer system, resonant states of the single δ-layers interact. Energetically higher states are more extended in the growth direction and thus interact more strongly, which leads to a significant subband splitting. Consequently, electrons in these states are supposed to produce those features that distinguish multilayers from single layers. However, electrons of different subbands show different mobilities and multisubband transport is difficult to analyze. Therefore, we concentrate on low metallic doping concentrations around $N_D = 5 \times 10^{11}$ cm^{-2}, which is not far above the metal-insulator transition, where typically two subbands are occupied. Sheet distances vary from sample to sample between $d = 17$ nm and $d = 100$ nm.

In a previous paper we reported about the real space transfer of electrons into the space between the layers when elevated electric fields are applied.[3] In this paper we will focus on the magnetotransport properties of δ-doped multilayers. The paper is organized as follows: in Sec. II the samples are introduced and experimental results are shown. Section III describes the theoretical results for the electronic properties of the samples obtained from self-consistent calculations. In Sec. IV, we develop a consistent physical picture of the observed transport phenomena. Classical effects, the Shubnikov–de Haas (SdH) effect, and the quantum Hall effect (QHE) are discussed separately.

II. EXPERIMENTS

A. Samples

The δ-doped GaAs samples were grown by molecular beam epitaxy on (001)-oriented surfaces of semi-insulating substrates. An 800-nm undoped GaAs buffer layer is followed by the stack of δ-doped planes as shown in Fig. 1(a). δ doping was achieved in a stop-wait-go procedure at 520 °C in order to minimize the segregation of Si dopants in the growth direction. Between eight and ten doping planes are separated by undoped GaAs layers each of the thickness d. The last δ layer is covered by an undoped buffer of thickness $2d$. In order to avoid the depletion of the uppermost δ layer due to surface states, a thin volume doped cap layer was deposited on top. In Table I, the parameters of the three samples are listed.

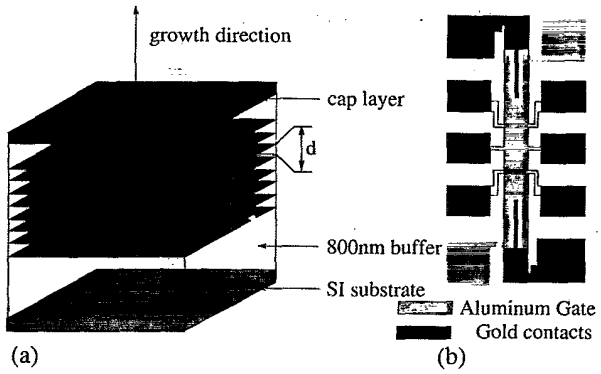

FIG. 1. (a) Samples. (b) Structures.

The Hall-bar structures depicted in Fig. 1(b) were etched using standard photolithography. An Al gate enabled us to control the electron density in the volume doped cap layer. Ohmic Au contacts served as source, drain, and as potential probes to measure ρ_{xx} and ρ_{xy}.

The samples were cooled down to 300 mK in an Oxford cryostat system. It was possible to apply a magnetic field up to 14 T normal to the sample surface. A source-drain current of not more than $I_{SD} = 100$ nA modulated with 15 Hz guaranteed the measurement of resistances in the Ohmic regime, which was performed with the lock-in technique.

The three samples have been grown to form a set with similar sheet-doping concentration but different sheet distance. It is convenient to introduce the "aspect ratio" $r = \langle a \rangle / d$, which is the ratio of the average donor spacing in the doping plane $\langle a \rangle$ divided by the layer spacing d. In the special case of sample C with $r = 1$, we have $\langle a \rangle = d$, which is similar to a homogeneously volume-doped sample showing the only difference of dopants ordered in the growth direction. Figure 2 shows the depth profile of the charge distribution in this sample obtained from a C-V measurement. On the left, the volume-doped cap layer can be identified, which is followed by the undoped buffer layer more to the right. The density peaks of the first two δ layers are clearly visible at the very right, which proves that dopant order in the growth direction was actually achieved.

B. Magnetotransport measurements

This section introduces the experimental methods and results and describes the characteristic features of the latter, which will be discussed in detail in a later section. The results of magnetotransport measurements for sample A are depicted in Fig. 3. The very pronounced QHE minimum in ρ_{xx} and the corresponding plateau in ρ_{xy} at $B > 10$ T enabled us to find the gate voltage that exactly depletes the volume-doped cap layer. If we have a number of N δ layers, the condition for the exact depletion of the cap layer is

$$\rho_{xy} = \frac{h}{e^2}\frac{1}{\nu N} \quad \text{and} \quad \rho_{xx} \approx 0 \,,$$

with the filling factor ν. The filling factor can be deduced from the magnetic field at which the minimum in ρ_{xx} occurs and is determined to be $\nu = 2$. In sample A, the gate voltage that exactly depletes the cap layer is found to be $U_g = -1.4$ V, with a plateau value of $1/16 = 0.0625$ (in units of h/e^2) for $N = 8$. At smaller gate voltages, the cap layer acts as a parallel conductivity which changes plateau values in ρ_{xy} and suppresses the pronounced minimum in ρ_{xx}.

Certain aspects of the curves for $U_g = -1.4$ V have to be emphasized in order to be analyzed in a later section. At $B < 0.5$ T a negative magnetoresistance is observed, which is due to the effect of weak localization typical for a two-dimensional (2D) disordered system.[4,5] Strong oscillations occur in ρ_{xx} for 1 T $< B <$ 8 T. Most remarkable is the fact that pronounced plateaus occur in ρ_{xy} at $B < 4$ T. If one disregards the negative magnetoresistance and tries to average the quantum oscillations in ρ_{xx} with the eye, a parabolic positive magnetoresistance remains for $B < 2$ T, which becomes weaker at higher fields. This comes along with a Hall curve that is bent at about $B = 2$ T.

In sample B, the sheet distance compared to sample A is reduced from $d = 100$ nm to $d = 40$ nm keeping the sheet-doping concentration almost constant. The magnetotransport data in Fig. 4 show that it is not possible to find any gate voltage at which the QHE minimum around $B = 12$ T drops down to zero. However, the sample is designed in such a way that the cap layer is depleted again at $U_g = -1.4$ V. We can therefore be sure that the supression of the QHE is a consequence of the reduced sheet distance. Furthermore, there are only feeble oscillations in ρ_{xx} and no plateaus in ρ_{xy} for 1 T $< B <$ 8 T. The remaining features are the negative magnetoresistance at $B < 0.5$ T and the parabolic positive magnetoresistance at $B < 2$ T with saturation at higher magnetic fields. The latter is even better visible than in sample A since the quantum oscillations are rather weak.

If we proceed to sample C, which has the further increased aspect ratio of $r = 1$ (Fig. 5), we again find no QHE at high magnetic fields, but clear SdH oscillations can be seen. This would also be expected in a corresponding volume-doped sample. Contrary to sample B, there is no positive magnetoresistance any more but a

TABLE I. Sample parameters.

Sample	No. of δ layers	Sheet distance (nm)	Sheet-doping conc. (10^{11} cm^{-2})	"Aspect ratio"
A	8	100	5.4	0.14
B	8	40	5.0	0.35
C	10	17.1	3.4	1

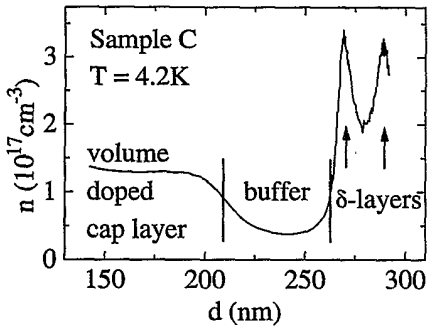

FIG. 2. Depth profile of the charge density in sample C obtained from a *C-V* measurement.

weak negative magnetoresistance over the whole range of magnetic fields.

III. ENERGY LEVELS AND TOTAL DENSITY OF STATES

In order to describe the electronic properties of δ-doped layers appropriately, it is necessary to use a self-consistent model in the effective mass approximation. In this model, the donor charge in each δ-doped layer is represented by a homogeneously charged plane (jellium model). Thus, potential fluctuations due to the spatial discreteness of the donor charges are neglected. We determined the electron distribution in an effective potential in growth direction either by solving the one-electron Schrödinger equation and using Fermi statistics or, alternatively, by using the Thomas-Fermi approximation (TFA). The effective potential is determined solving the Poisson equation and adding a local exchange-correlation contribution calculated in the local-density approximation (LDA) after Gunnarsson and Lundqvist.[6]

The differences between the TFA, the Hartree approximation (HA), and the LDA are most easily understood in terms of the density functional formalism of Hohenberg and Kohn,[7] and Kohn and Sham.[8] In the TFA, the Coulomb interaction between electrons is completely neglected and the kinetic energy of the system is approximated by that of a free electron gas. In the HA, the latter

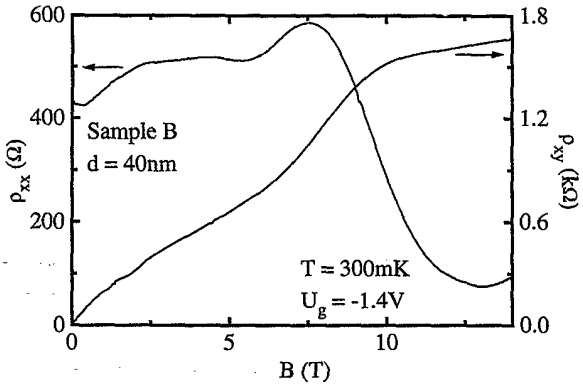

FIG. 4. Magnetoresistance and Hall resistance of sample B.

approximation is replaced by the full nonlocal quantum-mechanical expression. The LDA additionally accounts for many-particle effects by introducing a local exchange-correlation potential.

We want to show that the quantum-mechanical treatment of the kinetic energy *and* the inclusion of exchange-correlation effects is necessary to obtain the actual spatial density distribution at the doping concentrations under consideration. Figure 6 shows the effective potentials and the electron distributions according to the TFA, HA, and LDA for a part of a multilayer with $N_D = 5 \times 10^{11}$ cm^{-2} per doping sheet. The most significant differences occur in the region of the density peaks as well as in the interlayer space. The TFA always produces the unphysical sharp kink at the density peak, which is a direct result of the sharp kink of the potential in the doping plane. This is avoided in the HA or LDA by solving the Schrödinger equation. In the space between the δ layers, the TFA and HA lead to almost the same density, whereas it is significantly reduced there in the LDA. This is the effect of the exchange-correlation energy, which acts as an additional attractive potential marked as U_{xc} in the potential plot. U_{xc} can be neglected when the total exchange-correlation energy of the system is much smaller than the total kinetic energy. For the former $U_{xc} \propto n^{0.29}(\mathbf{r})$ is valid,[9] whereas for the latter we have $T \propto n_{tot}^2$ in a 2D electron gas. Thus, the higher the electron concentration, the less important is U_{xc} and vice versa. In metallic δ-doped sys-

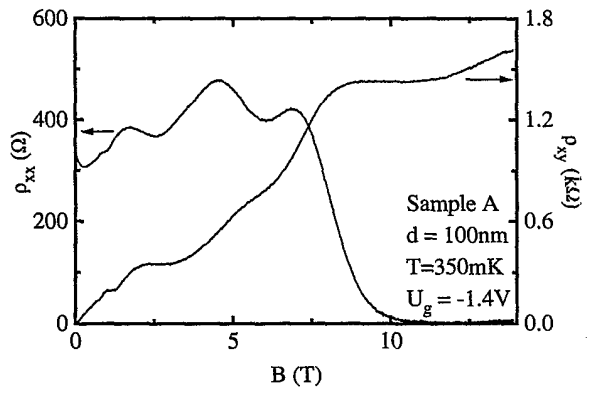

FIG. 3. Magnetoresistance and Hall resistance of sample A.

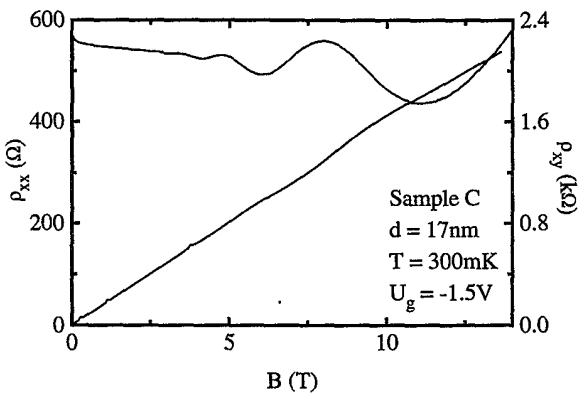

FIG. 5. Magnetoresistance and Hall resistance of sample C.

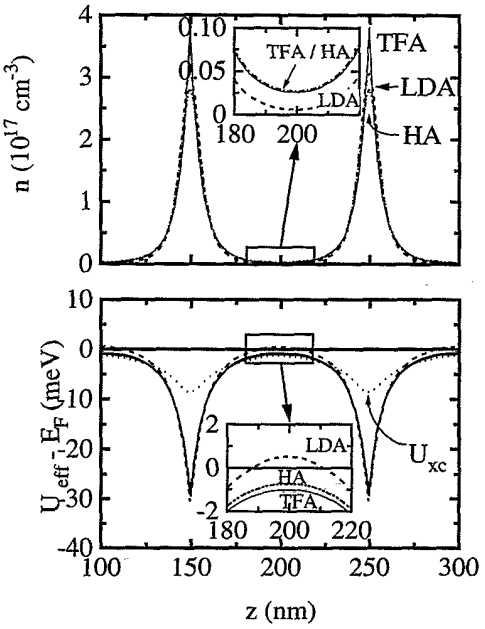

FIG. 6. Comparison between Thomas-Fermi approximation (TFA), Hartree-approximation (HA), and local-density approximation (LDA).

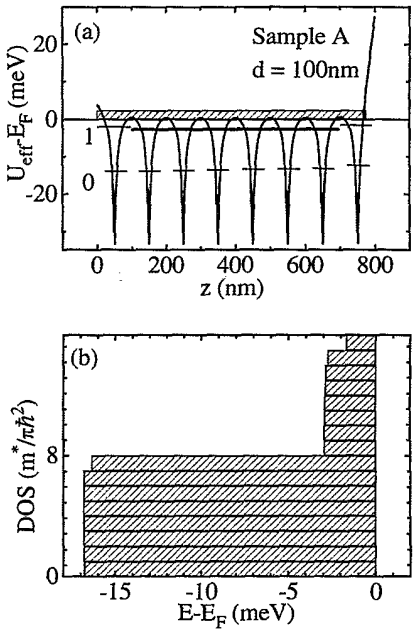

FIG. 7. Self-consistent calculations for sample A. Parameters are $N_D = 5.6 \times 10^{11}$ cm^{-2}, $N_A = 5 \times 10^{14}$ cm^{-3}, $T = 1.3$ K, $d = 100$ nm. (a) Effective potential and energy levels. (b) Density of states.

tems in our concentration region, exchange-correlation effects must not be neglected. This is why we have to use the LDA.

The subband physics of single layers in the jellium model is that of a one-dimensional atom. The higher the subband energy is, the more extended are the wave functions. In multilayers the resonant subbands of the individual wells interact, which leads to the splitting of a certain subband into a number of subband states equal to the number of the layers. The splitting of the more extended subbands is stronger than that of the states bound tightly to the doping planes. The quantum mechanics is that of a one-dimensional molecule. Thinking of a large number of δ layers one can — in analogy to superlattices — speak about the formation of minibands in a doping superlattice.

The subband structure and the density of states (DOS) was calculated for the three measured samples and is shown in Figs. 7–9. In sample A, one can distinguish two minibands (labeled 0 and 1) well below the Fermi level and a set of strongly split levels that are just at and above the Fermi level (see Fig. 7). The DOS is characterized by two large steps, each indicating the bottom of one of the subbands 0 and 1. This reflects the weak coupling between neighboring wells, which allows us to regard the system as composed of eight parallel but noninteracting two-dimensional electron gases with two occupied subbands in each of them.

In sample B, the sheet distance is reduced and consequently the splitting of the 1.subband is dramatically increased (see Fig. 8). The DOS reminds us of the DOS of a three-dimensional (3D) electron gas, which is added in the figure as a square root curve labeled with $\mathcal{D}_{3D}$. As a matter of fact, the self-consistent treatment of this structure leads to a dispersion E_n for this miniband, which is very well approximated by the eigenvalues of the particle-in-box problem

$$E_n = \frac{\hbar^2 \pi^2 n^2}{2 m_\perp W^2}, \quad n = 1, 2, 3, \ldots,$$

if we introduce the effective width of the sample $W = 340$

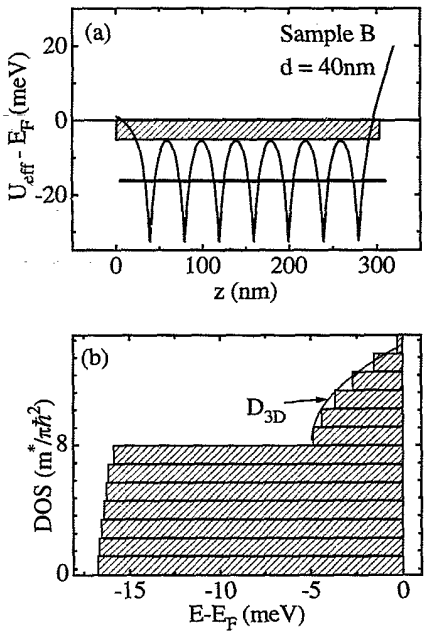

FIG. 8. Self-consistent calculations for sample B. Parameters are $N_D = 5.4 \times 10^{11}$ cm^{-2}, $N_A = 5 \times 10^{14}$ cm^{-3}, $T = 1.3$ K, $d = 40$ nm. (a) Effective potential and energy levels. (b) Density of states.

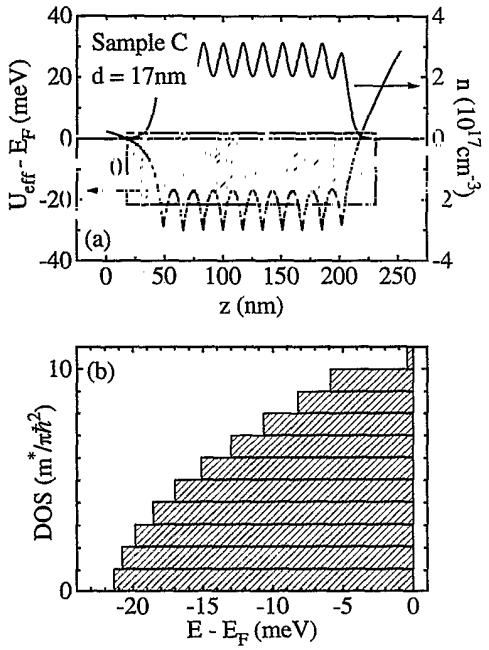

FIG. 9. Self-consistent calculations for sample C. Parameters are $N_D = 4.3 \times 10^{11}$ cm^{-2}, $N_A = 5 \times 10^{14}$ cm^{-3}, $T = 1.3$ K, $d = 17$ nm. (a) Effective potential, energy levels, and total electron density. (b) Density of states.

nm and a mass $m_\perp = 0.36m^*$ in growth direction. The effective width W is obtained from the envelopes of the lowest miniband states, which are simple sine-functions with wave vectors

$$K_z = \frac{\pi n}{W}.$$

Note that the indices n are counted from the bottom of this miniband. The periodically modulated bottom of the box leads to a renormalization of the effective mass in growth direction to a value, which is *smaller* than the effective mass parallel to the doping planes, e.g., the GaAs conduction band mass at the Γ minimum. Putting the definition of K_z into the expression for the energy gives the dispersion $E_z(K_z)$ of a free particle with mass $m_\perp$. There is also another way of looking at this subband. The wave functions in the z direction describe states in the artificial periodic potential of the doping layers. They can therefore be approximated with a Bloch function with the wave-vector K_z of a new quasiparticle. It has the dispersion of a free particle with the *effective mass* $m_\perp$, which is indeed smaller than the electron effective mass in the GaAs conduction band. The total dispersion is no longer isotropic and leads to the three-dimensional density of states $\mathcal{D}_{3D}$:

$$\mathcal{D}_{3D} = \frac{1}{2\pi^2}\frac{2m_\parallel}{\hbar^2}\left(\frac{2m_\perp}{\hbar^2}\right)^{1/2}\sqrt{E}, \qquad (1)$$

where $m_\parallel = m^*$. A comprehensive discussion of these models and the underlying physics is given elsewhere.[10]

In sample C, even the states of the 0.subband interact so strongly that their energies are strongly split and the DOS has the form of a 3D one. In this case, the analysis in terms of Bloch functions leads to the result $m_\perp = m^*$. This is no surprise since the potential variations in z direction are small compared to E_F, which lets the sample appear as volume doped. If we focus on the electron distribution in this sample, we find a nice agreement between the calculated and the measured results (compare Figs. 2 and 9).

The electrons in the 0.subband of samples A and B are bound closely to the doping plane. They screen the long-range part of the Coulomb potential of the donors and they are expected to have a low mobility. Electrons in the 1.subband move in a pseudopotential due to the orthogonality of subband states. They are further apart from the doping plane where most of the long-range scattering potential is screened. Thus, they are expected to have an enhanced mobility compared to the electrons in the 0.subband.

With respect to the discreteness of donor charges and the statistical disorder in their distribution, the jellium model is a zeroth-order approximation, which can be used as the basis for the inclusion of disorder effects. This has been done by Gold *et al.*[11,12] using a Green's-function approach. Disorder smears out the sharp steps of the 2D DOS. The fluctuation potential of the donors is screened by the electrons of the subbands so that only a short-range scattering potential determines the transport properties. At low temperatures, elastic scattering in this random impurity potential is the dominant scattering mechanism determining the low-field transport properties.

IV. ANALYSIS OF THE RESULTS

Measuring the conductivity at low temperatures probes the DOS at the Fermi level $\mathcal{D}(E_F)$ and the diffusion constant D^*, which is connected to the scattering time at the Fermi level $\tau(E_F)$.[13,14] In a magnetic field, the diffusion constant and the conductivity are no longer scalars but tensors.

A. Classical magnetotransport

The classical Boltzmann theory of magnetotransport assumes classical particles moving under the influence of the Lorentz force. The resulting conductivity is given by the well-known expression

$$\sigma = \frac{ne^2\tau/m^*}{1+(\omega_c\tau)^2}\begin{pmatrix} 1 & -\omega_c\tau \\ \omega_c\tau & 1 \end{pmatrix}, \qquad (2)$$

with the electron concentration n, the scattering time τ, the effective mass m^*, and the cyclotron frequency in a magnetic field of strength B given by $\omega_c = eB/m^*$. The resistivity is the matrix inverse of the conductivity:

$$\rho = \frac{m^*}{ne^2\tau}\begin{pmatrix} 1 & \omega_c\tau \\ -\omega_c\tau & 1 \end{pmatrix},$$

which means that ρ_{xx} is independent of the magnetic field and ρ_{xy} depends linearly on B. This classical model explains the magnetotransport in sample C, if we average

the oscillatory part of ρ which will be discussed later. In this sample we have an almost constant ρ_{xx} and a ρ_{xy}, which increases linearly in B.

However, this simple classical model does not explain the magnetotransport properties of the samples A and B, which have a positive magnetoresistance at low fields which saturates at intermediate B. If we consider the results of the self-consistent calculations, the main difference to sample C is the existence of two occupied subbands. We can argue that the current contributions of the two subbands might add and so do the conductivities. This would lead to

$$\sigma_{xx} = \frac{e^2}{m^*}\sum_{i=1}^{2}\frac{n_i\tau_i}{1+(\omega_c\tau_i)^2} = \frac{e^2}{m^*}\mathrm{Re}\left\{\mathrm{Tr}\left[\mathbf{N}\left(\mathbf{K}-i\omega_c\right)^{-1}\right]\right\}, \tag{3a}$$

$$\sigma_{xy} = \frac{e^2}{m^*}\sum_{i=1}^{2}\frac{n_i\omega_c{\tau_i}^2}{1+(\omega_c\tau_i)^2} = \frac{e^2}{m^*}\mathrm{Im}\left\{\mathrm{Tr}\left[\mathbf{N}\left(\mathbf{K}-i\omega_c\right)^{-1}\right]\right\}, \tag{3b}$$

with the elements of the density matrix $N_{ij} = n_i\delta_{ij}$ and the elements of the scattering matrix $K_{ij} = {\tau_i}^{-1}\delta_{ij}$. The notation, which makes use of the scattering and the density matrix, seems to be a little complicated to express the simple facts, but it will turn out immediately to be very powerful.

As a matter of fact, the argumentation above disregards the effects of scattering between different subbands, the intersubband scattering. The Boltzmann equation can be solved in the relaxation time approximation including intersubband scattering.[15] The result is a conductivity tensor that can be written in the same form with $\mathbf{N}$ and $\mathbf{K}$ as in Eq. (3), with the difference that now $N_{ij} = \sqrt{n_i n_j}$ and $\mathbf{K}$ has off-diagonal elements with the property $K_{ij} = K_{ji}$.[16] It is noteworthy that in this description not only the off-diagonal, but also the diagonal parts of $\mathbf{K}$ contain contributions of the intersubband scattering. This classical theory can now be applied to the experimental data. As a classical theory will always do, it averages the quantum-mechanical oscillations.

In order to reduce the number of adjustable parameters, we calculated the scattering matrix for a single δ layer with two occupied subbands. For this purpose the static inverse dielectric function ε^{-1} was calculated in the random-phase approximation using the quantum-mechanical wave functions from the self-consistent calculations. Then the screened scattering potential, which is the screened potential of ionized Si donors, can be written as[15]

$$\phi_{ij}(\mathbf{q}) = \sum_{lm}\varepsilon^{-1}_{(ij)(lm)}(\mathbf{q})V^{(\mathrm{imp})}_{lm}(\mathbf{q}).$$

Here $\phi_{ij}(\mathbf{q})$ denotes the matrix elements of the screened and $V^{(\mathrm{imp})}_{lm}(\mathbf{q})$ the one of the unscreened scattering potential. Impurity charges were assumed to be δ correlated in an infinitely thin doping plane. It turns out that the off-diagonal matrix elements of the scattering matrix $\mathbf{K}$ are very small compared to the diagonal ones. Therefore, it is appropriate to regard the scattering matrix to be diagonal, which means that the total conductivity can in fact be described as the sum of separate contributions of the two subbands. However, this does *not* mean that intersubband scattering is completely neglected, since also the diagonal elements of the scattering matrix $\mathbf{K}$ contain intersubband contributions.

In order to get further orientation in the fitting procedure of experimental data, the subband densities obtained from the self-consistent calculations were used as a clue to reduce the range of free parameters. Figure 10 shows the result graphically and Table II lists the parameters which were the average of different reasonable fits.

B. The SdH effect

In order to analyze the oscillatory behavior of the magnetoresistance, it is convenient to dig out the oscillations using the following technique. At first the measured resistivity tensor is inverted to obtain the conductivity tensor. Then the part is substracted, which can be obtained in the classical framework of the two carrier model. What remains is the pure oscillatory part of the conductivity.

This method of analysis is justified by theoretical results of a number of authors.[17–19] They all find results for the conductivity of the form

$$\sigma_{xx}(B) = \sigma^{(\mathrm{class})}_{xx} \times\left[1+A\exp\left(-\frac{\pi}{\omega_c\tau_s}\right)\cos\left(\frac{2\pi E_F}{\hbar\omega_c}\right)\right], \tag{4a}$$

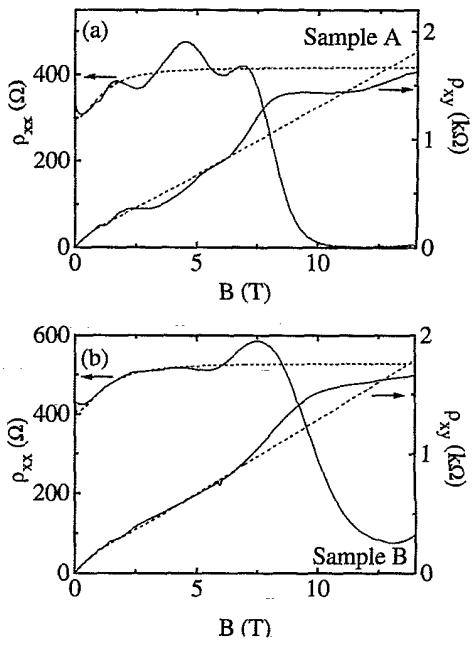

FIG. 10. Classical magnetoresistance and Hall resistance of a two-carrier system compared with the experimental data. (a) Sample A. (b) Sample B.

TABLE II. Densities and mobilities from the classical model.

Sample	K_{11} (meV)	K_{22} (meV)	K_{12} (meV)	μ_0 (cm^2/Vs)	μ_1 (cm^2/Vs)	n_0 (10^{11} cm^{-2})	n_1 (10^{11} cm^{-2})
A	7.57	1.38	-0.07	2330	12818	4.90	0.93
B	7.83	1.53	-0.15	2279	12004	5.53	0.54
Calculated (Single layer)	7.74	1.52	-0.005	2236	11352	4.24	0.68

$$\sigma_{xy}(B) = \sigma_{xy}^{(\mathrm{class})} \times \left[1 - B\exp\left(-\frac{\pi}{\omega_c\tau_s}\right)\cos\left(\frac{2\pi E_F}{\hbar\omega_c}\right)\right], \quad (4b)$$

where the classical quantities are given by Eq. (2), E_F is the Fermi energy, and τ_s is the single-particle relaxation time. Equation (4) tells us that the SdH oscillation is superimposed on the classical conductivity. Laikhtman and Altshuler[19] found from their calculations that the scattering time τ in Eq. (2) is the momentum relaxation time (or transport lifetime) τ_t. In former theories no distinction between τ_s and τ_t had to be made, since only short-range δ scatterers had been considered leading to $\tau_s = \tau_t \equiv \tau$. The prefactors A and B in Eq. (4) can be written as the product of a temperature dependent and a temperature independent part[19] when the self-consistent Born approximation (SCBA) is used:

$$A = 2C(T)\frac{1-(\omega_c\tau_t)^2}{1+(\omega_c\tau_t)^2},$$

$$B = C(T)\frac{4}{1+(\omega_c\tau_t)^2},$$

$$C(T) = \frac{2\pi^2 T/\hbar\omega_c}{\sinh(2\pi^2 T/\hbar\omega_c)}.$$

In the same sense as the 3D DOS can be generated by the superposition of a large number of 2D states in a large volume, the SdH effect in a 3D system can be understood as a superposition of the oscillations of many 2D subbands.[20] Therefore, the same arguments are also valid for 3D systems, with the only difference that summing up many oscillating functions with different periods will result in a phase shift of the total oscillation.[21]

Figures 11–13 show the results of the procedure discussed above. Also shown are the results that one would expect using the SCBA results of Laikhtman. Integer filling factors are marked by arrows.

Sample A exhibits a satisfactory agreement of the extracted density and mobility of the first subband, the results of the model calculation, and the transport parameters obtained with the classical analysis (see Table III). If one follows the phase relation between $\Delta\sigma_{xx}$ and $\Delta\sigma_{xy}$, one finds that they have a phase difference of π at low fields as expected from Eq. (4). At higher magnetic fields, this phase difference changes to a value of about $\pi/2$. According to Coleridge and Stoner[22] such a shift of the phase difference should be considered as a signature of localization, which is a necessary condition for the QHE. Laikhtman claimed that there is a boundary between the quantum Hall regime and the SdH oscillations determined by the condition

$$\omega_c\tau_s = \frac{\pi}{2}. \quad (5)$$

For our sample A, this boundary is at $B \approx 1.76$ T or $1/B \approx 0.57$ T^{-1} indicating that the minimum with $\nu = 2$ could also be a quantum Hall minimum. However, there is still the parallel conductivity of the 0.subband, which shows no quantum phenomena at these low fields since the electrons have a quite low mobility. Thus, localized states of the 1.subband are in resonance with delocalized states of the 0.subband. Consequently, we cannot expect σ_{xx} to vanish in the 1.subband, since intersubband scattering is possible.[23]

The SdH oscillations in sample B, which were hardly visible in the measured curves, are clearly visible after the subtraction of the classical contribution. In Fig. 12 we show the derivative of $\Delta\sigma_{xx}$ with respect to $1/B$ in

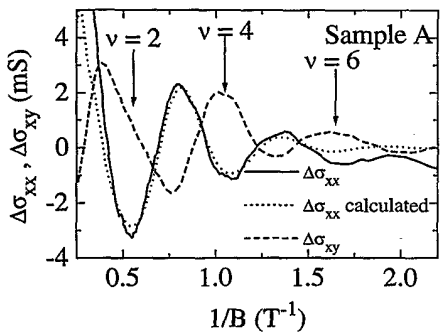

FIG. 11. SdH oscillations of the 1.subband in sample A.

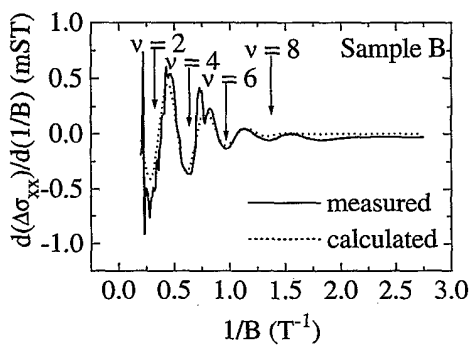

FIG. 12. SdH oscillations of sample B. The calculated curve is a superposition of contributions of the subbands that form the 1.miniband. The superposition accounts for the characteristic phase shift of the oscillations (see text).

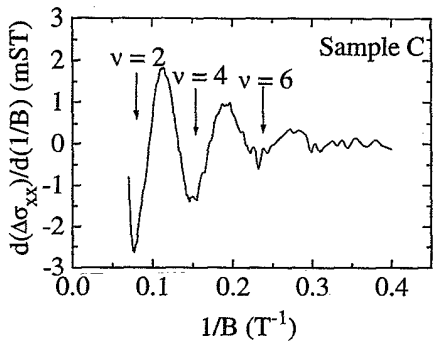

FIG. 13. SdH effect in sample C.

order to make clear that there is a phase shift of $\pi/2$ compared to sample A. Minima at the integer filling factors $\nu = 2, 4, 6, 8$ appear in $\frac{d(\Delta\sigma_{xx})}{d(1/B)}$ rather than in $\Delta\sigma_{xx}$. This phase shift can be understood by direct application of the theory of Adams and Holstein for 3D systems[21] or, equivalently, by the superposition of the oscillations in the SCBA due to 2D subbands weighted with the subband densities from the self-consistent calculation. This indicates that the 1.subband in sample B has undergone the transition towards a 3D band as supposed from the self-consistent calculation. The Fermi energy determined from the period of the oscillations is indeed in very good agreement to theory.

In sample C we find SdH oscillations with the same phase shift as in sample B (Fig. 13). Here, however, it is the strongly split 0.subband that exhibits a 3D character. The Fermi level determined from the period of the oscillations in this sample is also in excellent agreement with the self-consistent calculation. In Table III the Fermi levels and carrier densities are listed, which were extracted from the SdH effect in the three samples.

C. Quantum Hall effect

A proper QHE is only observed in sample A with a sheet distance of 100 nm. In sample B, the plateau in ρ_{xy} at $B \approx 12$ T is not flat and ρ_{xx} is not very small compared to other fields. Considering Eq. (5), nevertheless, one can attribute the QHE with the filling factor $\nu = 2$ to this minimum and deduce an electron density. Electron densities obtained for samples A and B are listed in Table IV. These densities are the *total* electron densities, e.g., the sum of both subbands. The reason for that is the magnetic depopulation of the upper subband at a certain magnetic field. The system always tends to have the lowest total energy possible. At zero magnetic field, it lowers the total energy of the system to form a second subband in spite of filling all the electrons into one subband. This increases the electrostatic energy of the system since electrons are further apart from the charged donors. At the same time, however, it lowers the kinetic energy of the carriers, which always prevails at sufficiently high densities. If a strong magnetic field is applied perpendicular to the doping planes, the electrons fill the lowest Landau levels. These are shifted up in energy with increasing magnetic field, but at the same time can accommodate more electrons since the Landau level degeneracy increases. At a certain magnetic field, the system can lower its total energy by redistributing electrons from the lowest Landau level of the 1.subband to that of the 0.subband. This effect was already observed in cyclotron resonance experiments on $Al_xGa_{1-x}As$-GaAs quantum well structures.[24]

One can easily introduce the perpendicular magnetic field into the self-consistent calculation, since it does not couple the in-plane with the perpendicular motion. Therefore, the magnetic field only enters the calculation of the electron density for each subband. One has to integrate the Landau DOS $\mathcal{D}_L$ multiplied with the Fermi-Dirac distribution function $f(E)$:

$$n(z, E_F) = \sum_i \left|\varphi_z^{(i)}(z)\right|^2 \int_0^\infty dE \mathcal{D}_L(E) f(E_i + E - E_F) \; .$$

Figure 14 shows the effect of the magnetic depopulation of the first subband in sample A as the result of a self-consistent calculation. For this calculation we used a Landau DOS with Gaussian broadening.[25]

Still the question is open why the QHE is suppressed in sample B. A crucial condition for the existence of the QHE is the absence of scattering at integer filling factors. If we take the splitting of energy levels due to the interaction of neighboring sheets as a measure of the interaction between layers, we find a value of less than 10 μeV for sample A and a value of about 0.6 meV for sample B. This indicates that in the latter sample interlayer scattering might be important even for the 0.subband thus suppressing the QHE. From the superlattice point of view,[26] a higher subband splitting (higher miniband width) means a lower effective mass for the motion through the barriers, which means a higher kinetic energy of the carriers in the z direction. The QHE is only observable when this kinetic energy is sufficiently low compared to $\hbar\omega_c$.

However, we have to take into account that the low carrier mobility in δ layers compared to electrons in su-

TABLE III. Fermi levels and subband occupations obtained from the SdH oscillations. The calculated values for the Fermi levels are also shown.

Sample	E_F (meV)		n_1^{2D} (10^{11} cm^{-2})	n_0^{3D} (10^{16} cm^{-3})	n_1^{3D} (10^{16} cm^{-3})
	meas.	calc.			
A	3.15	3.05	0.886		
B	4.94	4.98	0.703		1.65
C	21.93	21.5	0	25.6	0

TABLE IV. Electron concentrations obtained from the QHE.

Sample	$n^{(QHE)}$ (10^{11} cm^{-2})
A	5.8
B	5.9

perlattices leads to a significant smearing out of the steps in the 2D DOS and to a significant Landau level broadening. The typical energy for these changes of the electron spectrum due to disorder is $\hbar/\tau$, which is in any case much larger than the subband splitting. Implications of the latter are therefore rather unimportant compared to the broadening of the DOS. Therefore, we believe a different mechanism to be responsible for the suppression of the QHE in sample B. The quasi-3D DOS of the 1.subband depicted in Fig. 8(b) will have a low energy tail due to disorder in realistic samples. Electrons occupying these states can percolate in all directions even at high magnetic fields. We suggest that scattering of electrons into these states suppresses the QHE.

V. CONCLUSIONS

We have shown that the distance d of the δ layers in a metallic multilayer system is a crucial parameter that determines the system properties. Decreasing the layer distance has two effects: First, subbands are split more strongly and shifted up in energy. The smaller d the less subbands are occupied. Second, the strong splitting of the subband states is equivalent to the transition from a 2D to a 3D transport behavior. Our samples had been designed in such a way that we were able to analyze the magnetotransport data obtaining a conclusive and complete picture of the physical phenomena. The 3D nature of subbands was proven through a phase shift in the SdH oscillations and the suppression of the QHE. In the sample in which two 2D subbands are occupied, we found a magnetic depopulation of the upper subband.

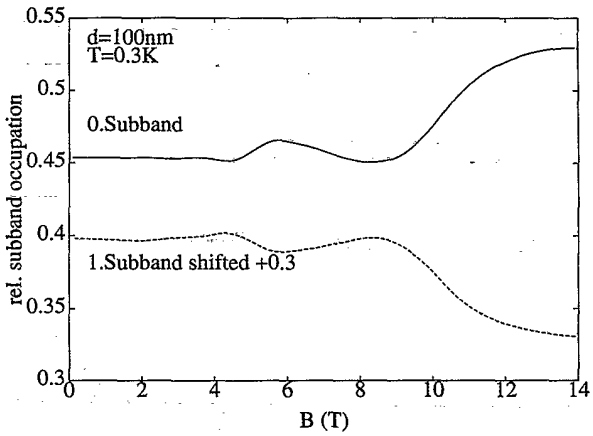

FIG. 14. Relative subband densities for sample A obtained from a self-consistent calculation. The magnetic depopulation of the 1.subband begins at $B \approx 9$ T.

ACKNOWLEDGMENTS

We thank R. Zimmermann for helping to develop the program for the self-consistent calculation and S. Riedel and E. Wiebicke for technical assistance and sample preparation. We also acknowledge useful discussions with M.E. Raikh and K. Karrai. This work was supported by the Deutsche Forschungsgemeinschaft DFG.

* Present address: Department of Physics, University of Nottingham, University Park, Nottingham NG7 2RD, England.

[1] F. Koch, in *High Magnetic Fields in Semiconductor Physics III*, edited by G. Landwehr, Springer Series of Solid State Sciences 101 (Springer-Verlag, Berlin, 1992), p. 377.
[2] F. Koch and A. Zrenner, Mater. Sci. Eng. B **1**, 221 (1989).
[3] H. Kostial *et al.*, Phys. Rev. B **47**, 4485 (1993).
[4] M. Asche, K.J. Friedland, P. Kleinert, and H. Kostial, Semicond. Sci. Technol. **7**, 923 (1992).
[5] J.J. Mares *et al.*, Phys. Rev. B **50**, 5213 (1994).
[6] O. Gunnarsson and B.I. Lundqvist, Phys. Rev. B **13**, 4274 (1976).
[7] P. Hohenberg and W. Kohn, Phys. Rev. **136**, B864 (1964).
[8] W. Kohn and L.J. Sham, Phys. Rev. **140**, A1133 (1965).
[9] M. Roesler, R. Zimmermann, and W. Richert, Phys. Status Solidi B **121**, 609 (1984).
[10] Th. Ihn, F. Koch, C. Gauer, and J.P. Kotthaus (unpublished).
[11] A. Gold, J. Serre, and A. Ghazali, Phys. Rev. B **37**, 4589 (1988).
[12] A. Gold, A. Ghazali, and J. Serre, Semicond. Sci. Technol. **7**, 972 (1992).
[13] R. Kubo, J. Phys. Soc. Jpn. **12**, 570 (1957).
[14] C.W.J. Beenakker and H. van Houten, in *Solid State Physics; Advances in Research and Applications*, edited by H. Ehrenreich and D. Turnbull (Academic Press, New York, 1991), Vol. 44, p. 1.
[15] T. Ando, A.B. Fowler, and F. Stern, Rev. Mod. Phys. **54**, 437 (1982).
[16] E. Zaremba, Phys. Rev. B **45**, 14 134 (1992).
[17] T. Ando, J. Phys. Soc. Jpn. **37**, 1233 (1974).
[18] A. Isihara and L. Smrčka, J. Phys. C **19**, 6777 (1986).
[19] B. Laikhtman and E.L. Altshuler, Ann. Phys. (N.Y.) **232**, 332 (1994).
[20] D. Schoenberg, *Magnetic Oscillations in Metals* (Cambridge University Press, Cambridge, England, 1984).
[21] E.N. Adams and T.D. Holstein, J. Phys. Chem. Solids **10**, 254 (1959).
[22] P.T. Coleridge and R. Stoner, Phys. Rev. B **39**, 1120 (1989).
[23] M.E. Raikh and T.V. Shahbazyan, Phys. Rev. B **49**, 5531 (1994).
[24] K. Ensslin, D. Heitmann, and K. Ploog, Phys. Rev B **37**, 10 150 (1988).
[25] R.R. Gerhardts, Surf. Sci. **58**, 227 (1976).
[26] H.L. Störmer *et al.*, in *Physics of Semiconductors: Proceedings of the 18th International Conference, Stockholm, Sweden*, 1986, edited by O. Engström (World Scientific, Singapore, 1987), p. 385.